Quantum Science and Technology

PAPER • OPEN ACCESS

Controlled expansion of shell-shaped Bose–Einstein condensates

To cite this article: Patrick Boegel *et al* 2023 *Quantum Sci. Technol.* **8** 034001

View the article online for updates and enhancements.

You may also like

- Flow mediated dilation with photoplethysmography as a substitute for ultrasonic imaging
G Mashayekhi, E Zahedi, H Movahedian Attar et al.
- Dissecting the Phase Space Snail Shell
Zhao-Yu Li and Juntai Shen
- Shell-shaped condensates with gravitational sag: contact and dipolar interactions
Maria Arazo, Ricardo Mayol and Montserrat Guilleumas

This content was downloaded from IP address 129.247.247.240 on 02/06/2023 at 08:53

IOP Publishing Quantum Sci. Technol. 8 (2023) 034001 https://doi.org/10.1088/2058-9565/acc969

Quantum Science and Technology

OPEN ACCESS

RECEIVED
10 September 2022

REVISED
10 March 2023

ACCEPTED FOR PUBLICATION
31 March 2023

PUBLISHED
27 April 2023

Original Content from this work may be used under the terms of the Creative Commons Attribution 4.0 licence.

Any further distribution of this work must maintain attribution to the author(s) and the title of the work, journal citation and DOI.

PAPER

Controlled expansion of shell-shaped Bose–Einstein condensates

Patrick Boegel[1,*], **Alexander Wolf**[2], **Matthias Meister**[2] **and Maxim A Efremov**[1,2]

[1] Institut für Quantenphysik and Center for Integrated Quantum Science and Technology (IQST), Universität Ulm, D-89081 Ulm, Germany

[2] German Aerospace Center (DLR), Institute of Quantum Technologies, D-89081 Ulm, Germany

[*] Author to whom any correspondence should be addressed.

E-mail: patrick.boegel@uni-ulm.de

Keywords: Bose–Einstein condensate, shell-shaped quantum gases, matter-wave lensing, radio-frequency dressing

Abstract

Motivated by the recent experimental realization of ultracold quantum gases in shell topology, we propose a straightforward implementation of matter-wave lensing techniques for shell-shaped Bose–Einstein condensates. This approach allows to significantly extend the free evolution time of the condensate shell after release from the trap and enables the study of novel quantum many-body effects on curved geometries. With both analytical and numerical methods we derive optimal parameters for realistic schemes to conserve the shell shape of the condensate for times up to hundreds of milliseconds.

1. Introduction

Many-body physics on shell topology has recently experienced a huge progress with the first creation of shell-shaped quantum gases [1, 2]. Inspired by the near-term availability of this novel topology, theoretical research has lead to new insights into quantum phenomena such as vortices [3–5], the Berezinskii–Kosterlitz–Thouless transition [6, 7], and the impact of dimensional as well as topological crossovers on the excitation spectrum [8, 9]. Consequences of the system being forced on a curved manifold may also influence ultracold chemistry [10] and few-body physics [11, 12], for example, in the form of confinement induced resonances [13–15].

Experimentally, two schemes have currently shown to be capable of creating shells: (i) radio-frequency (rf) dressing [16–20] in combination with a microgravity environment [1, 21], and (ii) an optically confined mixture of two Bose–Einstein condensates (BECs) employing a magic laser wavelength for trapping the mixture [2, 22, 23]. The latter scheme could also be realized in microgravity [22] and typically relies on a Feshbach resonance [24, 25] to tune the interspecies interaction that builds up the shell.

Although it is a stunning accomplishment that both schemes can produce shells of quantum gases, it is still hard to realize rather large shells while maintaining relevant atom–atom interactions to truly observe many-body phenomena [1, 26]. In fact, the current approaches allow only limited access to tune the interspecies interaction of atoms in the shell via Feshbach resonances while being trapped. This restriction is due to the fact that the rf-dressing approach requires position dependent magnetic fields together with constant rf fields to generate the trapping potential and, therefore, there is no freedom to apply another homogeneous magnetic field to take advantage of Feshbach resonances. Likewise, for the case of an optically trapped dual-species mixture, a specific magnetic background field is already required for most isotope combinations to adjust the repulsive interaction between the two species to form the shell in the first place. Consequently, additional Feshbach resonances can in general be applied only during free expansion of the shell after completely switching off the trap. However, without a confinement, the matter-wave dynamics of the released shell generally leads to a rapid increase of its thickness due to the atoms moving both outwards and inwards. Thus, observing shell-related many-body physics would usually be limited to few tens of milliseconds, until the atoms have reached the center and the shell structure is lost [2, 22, 26, 27].

© 2023 The Author(s). Published by IOP Publishing Ltd

In order to overcome these restrictions we explore in this article the application of matter-wave lensing techniques [28–33] to shell-shaped BECs. By preparing a free expansion in which the shell structure is conserved for hundreds of milliseconds, we allow for sufficient time to further manipulate the atom cloud with free fields, e.g. by using magnetic Feshbach resonances or laser light. In particular, attractive interactions between the atoms could be used to further reduce and control the width of the shell dynamically or to enable the study of few-body effects, losses and molecule formation in curved geometries. Moreover, with our approach free expanding shells of quantum gas could be used as the starting point for atom interferometers to built novel quantum sensors which typically scale favorably with extended free evolution times.

Here we propose two schemes with their applicability depending on the setup initially used to prepare the shell: (i) delta-kick collimation (DKC) [29–33] relies on switching on the original trapping potential for a short time during free expansion to reduce the width of the momentum space distribution at the expense of a larger position space distribution which is well suited for optically confined mixtures, and (ii) excitation induced collimation [28, 32, 34], where a swift change of the trap parameters is used to induce an oscillation in the thickness of the shell before switching off the trap close to the point of maximum thickness. The latter is specifically designed to be used in setups based on rf dressing that do not allow the trapping potential to be switched completely off and on again at will due to mixing of different magnetic hyperfine sublevels. By deriving optimal conditions for the collimation sequence, we show that both techniques are capable of conserving the shell structure for several hundreds of milliseconds which can be used for extensive probing of the system.

This article is structured as follows. In section 2 we introduce an effective model to describe both the ground state and dynamics of a large spherically symmetric shell-shaped BEC, which can also be used as a powerful tool for future studies of shell-shaped quantum gases. Starting from the three-dimensional (3D) nonlinear Gross–Pitaevskii equation (GPE), we discuss two approximations to reduce the equation of motion to a one-dimensional (1D) linear Schrödinger equation and present a general analytic solution which is employed throughout the article. The DKC-inspired approach for lensing of shell-shaped BECs is presented in section 3, where we focus on controlling the thickness of the shell during its free expansion by varying multiple parameters involved in the process. Using our effective model, we derive conditions to conserve the shell structure for the longest possible times. At the end of the section a generalized version of DKC is discussed that can be used to describe excitation induced collimation. In section 4 we consider the application of an adapted scheme to rf-dressed potentials, where any change of the parameters needs to be reasonably adiabatic in order to not mix different magnetic hyperfine sublevels. We show that even with these restrictions the expansion dynamics of shell-shaped BECs can be controlled with similar success as in the DKC case. Our conclusion in section 5 is followed by two appendices which present the effective 1D model in detail. Appendix A contains an in-depth discussion concerning the approximations needed to apply the 1D model instead of the 3D GPE, whereas appendix B summarizes the analytical solutions derived for different time-profiles of the employed sequences.

2. Shell-shaped BECs

In this section we first present the general framework to study shell-shaped BECs with the 3D GPE and then introduce an analytical model based on the 1D Schrödinger equation, that enables an efficient description of the ground state and dynamics of shell-shaped BECs valid in the limit of large shell radius.

2.1. System under study

To describe a BEC consisting of N atoms of mass m, in an external potential $V(\mathbf{r},t)$, we use the 3D nonlinear GPE

$$\mathrm{i}\hbar\frac{\partial}{\partial t}\psi(\mathbf{r},t)=\left[-\frac{\hbar^2}{2m}\nabla^2+V(\mathbf{r},t)+\frac{4\pi\hbar^2 a_s}{m}N|\psi(\mathbf{r},t)|^2\right]\psi(\mathbf{r},t) \tag{1}$$

for the macroscopic wave function $\psi=\psi(\mathbf{r},t)$ which is normalized according to the condition

$$\int \mathrm{d}^3r|\psi(\mathbf{r},t)|^2=1, \tag{2}$$

where $\mathbf{r}\equiv(x,y,z)$ is the position vector with the Cartesian coordinates x, y and z. Here we assume that the atoms are interacting via a contact potential whose strength is determined by the s-wave scattering length a_s.

In order to realize shell-shaped quantum gases two alternatives offer themselves which have both been demonstrated experimentally: either employing rf-dressing techniques to realize a bubble potential

[1, 16, 18], or taking advantage of the tuneable inter-species interaction in a dual-species BEC mixture to achieve a core–shell density distribution [2, 22]. In both cases the shell condensate effectively experiences a bubble potential which can be approximated by the form

$$V(\mathbf{r},t) \equiv \frac{m\omega_0^2}{2}\left[f(t)\right]^2\left(|\mathbf{r}|-r_0\right)^2 \tag{3}$$

corresponding to a spherically symmetric harmonic potential with its minimum at the radial position r_0 and the time-dependent frequency $\omega_0 f(t)$, determined by the frequency amplitude ω_0 and the scaling function $f(t)$. By changing r_0 and ω_0 the initial diameter and thickness of the shell can be controlled, respectively. Moreover, the time-dependent function $f(t)$ is used to dynamically adjust the width of the shell potential and is the key parameter for controlling the expansion dynamics of shell-shaped BECs in this article.

2.2. Analytical model for large quantum gas shells

The GPE is a nonlinear partial differential equation involving three spatial and one temporal variables and generally it is not easy to solve analytically. By using the fact that the trapping potential $V(\mathbf{r},t)$, equation (3), only depends on the radial coordinate $r \equiv |\mathbf{r}|$ and time t, we can consider spherically symmetric solutions of equation (1) and therefore effectively reduce the number of relevant spatial dimensions from three to one. Still, in this case the dynamics of a BEC is in general too complicated to be described with a reliable analytical model. Hence, in order to enable an analytical description and to apply it for finding the conditions of the optimal expansion of a shell-shaped BEC, we consider in this article the case where the shell radius is much larger than the thickness of the shell. This limit is reached when the minimum r_0 of the trapping potential equation (3) is much larger than the characteristic size $a_{\mathrm{HO}} \equiv \sqrt{\hbar/m\omega_0}$ of the ground state in the harmonic oscillator of frequency ω_0. In this regime we can apply two approximations which simplify the underlying differential equations and enable an analytical treatment.

In appendix A.1 we have shown that for the ground state of a shell-shaped BEC the atom–atom interaction becomes negligible for large shell radius, more precisely for $r_0 \gg \sqrt{Na_s a_{\mathrm{HO}}}$. In other words, this inequality means that the atom–atom interaction term in equation (1), being of the order of $(4\pi\hbar^2 a_s/m)(N/V_{\mathrm{sh}})$ with the shell volume $V_{\mathrm{sh}} = 4\pi r_0^2 a_{\mathrm{HO}}$, is small in comparison with the ground state energy $\hbar\omega_0$. Consequently, we can neglect the contribution from the interaction and use the 3D linear Schrödinger equation instead of the 3D nonlinear GPE to describe large shells.

When additionally $r_0 \gg a_{\mathrm{HO}}$, the ground state of a shell-shaped BEC can be well described by the stationary 1D Schrödinger equation, instead of the 3D version, as we have proven in appendix A.2. In this case the curvature of the shell is negligible and the system can be characterized with a single Cartesian position coordinate $x \in (-\infty, \infty)$ drastically reducing the complexity of the spatial derivatives in equation (1).

Thus, if $r_0 \gg \max\left\{a_{\mathrm{HO}}, \sqrt{Na_s a_{\mathrm{HO}}}\right\}$, it is sufficient to apply the 1D stationary Schrödinger equation to obtain the ground state of the system. In fact, in many practical implementations $Na_s \gg a_{\mathrm{HO}}$ such that neglecting the interaction is the stronger requirement. As a result, the optimal regime for applying our analytical model is the *non-interacting large-radius limit* which can be accessed with rather modest experimental parameters, as we have shown in appendix A.

It is worth noting that in this limit the width of the shell can still be considered relatively thick or rather thin depending on the ratio between the shell width and the healing length of the system. In both cases our model can be applied as long as the above inequalities hold, ensuring that interaction effects are negligible and the shell does not connect at the center of the coordinate system.

In order to model the dynamics of the shell-shaped BEC in the case of the time-dependent frequency $\omega_0 f(t)$, we use the 1D Schrödinger equation $(-\infty < x < \infty)$

$$\mathrm{i}\hbar\frac{\partial}{\partial t}\varphi(x,t) = \left\{-\frac{\hbar^2}{2m}\frac{\partial^2}{\partial x^2} + \frac{m\omega_0^2}{2}[f(t)]^2(x-r_0)^2\right\}\varphi(x,\tau) \tag{4}$$

for the wave function $\varphi(x,t) \equiv \sqrt{4\pi}x\psi(x,t)$ for $x \geqslant 0$, with $\psi(r,t)$ being the spherically symmetric solution of the 3D GPE (1) and r substituted by x. By comparing the analytical results obtained from equation (4) to the ones based on full 3D numerical simulations of the GPE, we show in section 3 that our 1D analytical model makes correct predictions as long as the atomic density $|\psi(\mathbf{r},t)|^2$ is zero around the origin, that is for $0 \leqslant r \lesssim a_{\mathrm{HO}}$, during the whole dynamics. This requirement is equivalent to being in the non-interacting large-radius limit.

2.3. Solutions for the dynamics of large shells

We can now show that the problem of solving the partial differential equation (4) can indeed be reduced to solving a linear ordinary differential equation which enables an efficient determination of the time-dependent width of the shell. In particular, according to appendix B, the general solution of equation (4) can be written analytically for any initial wave function $\varphi(x,0)$.

In our scheme, the shell-shaped BEC is initially prepared in a trapping potential $V(\mathbf{r},t)$ of the form of equation (3) with $f=1$ and $r_0 \gg \max\left\{a_{\mathrm{HO}}, \sqrt{N a_s a_{\mathrm{HO}}}\right\}$. According to appendix A, $\varphi(x,0)$ then coincides very well with the normalized wave function

$$\varphi(x,0) = \frac{1}{\left(\sqrt{\pi}a_{\mathrm{HO}}\right)^{1/2}} \exp\left\{-\frac{(x-r_0)^2}{2a_{\mathrm{HO}}^2}\right\} \tag{5}$$

of the ground state in the 1D harmonic oscillator.

Hence, the solution of equation (4) corresponding to this initial state reads

$$\varphi(x,t) = \frac{1}{\left(\sqrt{\pi}a_{\mathrm{HO}}\lambda\right)^{1/2}} \exp\left[-\left(\frac{1}{\lambda^2} - \mathrm{i}\frac{\dot{\lambda}}{\omega_0\lambda}\right)\frac{(x-r_0)^2}{2a_{\mathrm{HO}}^2} - \frac{\mathrm{i}}{2}\Phi\right], \tag{6}$$

where

$$\Phi(t) = \omega_0 \int_0^t \frac{\mathrm{d}t'}{[\lambda(t')]^2} \tag{7}$$

is a time-dependent phase factor and $\lambda = \lambda(t)$ with $\dot{\lambda} \equiv \mathrm{d}\lambda/\mathrm{d}t$.

The time-dependent function $\lambda(t)$ has to fulfill the corresponding Ermakov equation

$$\frac{\mathrm{d}^2}{\mathrm{d}t^2}\lambda + [\omega_0 f(t)]^2\lambda = \frac{\omega_0^2}{\lambda^3} \tag{8}$$

with the initial condition $\lambda(0)=1$ and $\dot{\lambda}(0)=0$.

Although the Ermakov equation (8) is a nonlinear ordinary differential equation of second order, its solution can be represented in terms of solutions of the corresponding linear differential equation. Indeed, as shown also in appendix B, the solution of equation (8) is given by

$$\lambda(t) = \sqrt{[\Lambda_1(t)]^2 + [\Lambda_2(t)]^2}, \tag{9}$$

where $\Lambda_1(t)$ and $\Lambda_2(t)$ are two linearly independent solutions of the linear differential equation

$$\frac{\mathrm{d}^2}{\mathrm{d}t^2}\Lambda + [\omega_0 f(t)]^2\Lambda = 0 \tag{10}$$

with the initial conditions $\Lambda_1(0)=1$ and $\dot{\Lambda}_1(0)=0$, and $\Lambda_2(0)=0$ and $\dot{\Lambda}_2(0)=\omega_0$.

From a physics view-point, the function $\lambda(t)$ defines the time dependence of the variance

$$\sigma^2(t) \equiv \langle x^2\rangle - \langle x\rangle^2 = \int_{-\infty}^{+\infty} x^2|\varphi(x,t)|^2\mathrm{d}x - r_0^2 = \frac{1}{2}[a_{\mathrm{HO}}\lambda(t)]^2 \tag{11}$$

of the position distribution $|\varphi(x,t)|^2$, with $\varphi(x,t)$ given by equation (6), corresponding to the width of the quantum gas shell. Here we have used the fact that the mean value of the position

$$\langle x\rangle(t) \equiv \int_{-\infty}^{+\infty} x|\varphi(x,t)|^2\mathrm{d}x = r_0 \tag{12}$$

is time-independent and coincides with the minimum of the trapping potential. Hence, the radius of the shell is constant during the dynamics.

Thus, the dynamics of a shell-shaped BEC trapped in the 3D harmonic potential equation (3) with large radius r_0 and, in particular, the time evolution of the shell width $\sigma(t)$ are solely determined by the solutions $\Lambda_1(t)$ and $\Lambda_2(t)$ of the linear differential equation (10) for a given frequency profile $f(t)$. In the following we apply this model to efficiently describe controlled expansion of shell-shaped BECs and to obtain optimal parameters for future experimental implementations.

3. Matter-wave lensing of shell-shaped BECs

In this section we analyze controlled expansion of shell-shaped BECs by applying the conventional DKC technique. Based on our 1D analytical model, we then derive the optimal parameters which allow us to keep both the shell radius and width almost constant for the longest possible free expansion times. Finally, we consider a more generalized scheme and discuss its applicability.

3.1. DKC with shell potentials

We start our analysis of shell-shaped BEC collimation from reminding the basic principles of the widely utilized scheme of DKC [28–33]. Indeed, this scheme consists of three steps: (i) a BEC prepared in a 3D harmonic potential is released from the trap at $t = 0$ and experiences a free expansion during the delay time t_d, (ii) the initial harmonic potential is turned on again for a short kick time t_k, and (iii) is switched off completely afterwards so that the BEC evolves freely. During the first step the BEC expands freely and increases its spatial size, accompanied by a conversion of interaction energy into kinetic energy. In the second step, the wave function of the BEC picks up a position-dependent phase proportional to the harmonic potential, similar to the well-known thin lens in optics. In this way, fast particles get a larger kick towards the center of the condensate compared to slower ones, resulting in a reduction of the width of the momentum distribution and consequently slowing down the expansion of the BEC.

Here we apply the DKC scheme to collimate a shell-shaped BEC by considering the following time profile

$$f_\mathrm{DKC}(t) = \begin{cases} 0, & 0 < t \leqslant t_\mathrm{d} \\ 1, & t_\mathrm{d} < t \leqslant t_\mathrm{d} + t_\mathrm{k} \\ 0, & t_\mathrm{d} + t_\mathrm{k} < t \end{cases} \tag{13}$$

for the trapping frequency of the bubble potential equation (3). Indeed, the scheme is fully determined by the delay time t_d and the kick time t_k while the strength of the kicking potential is chosen equally to the initial potential without loss of generality (see section 3.3).

In figure 1 we present the results of the delta-kick scheme, equation (13), with $t_\mathrm{d} = 30\,\mathrm{ms}$ and for different values of t_k, applied to the typical case of a ^{87}Rb BEC with $N = 10^5$ atoms, s-wave scattering length $a_s = 5.29\,\mathrm{nm}$, and trapping potential $V(\mathbf{r}, t)$ given by equation (3) with parameters $f(0) = 1$, $r_0 = 60\,\mu\mathrm{m}$ and $\omega_0 = 2\pi \cdot 50\,\mathrm{Hz}$. The solid lines in figure 1(a) represent the time evolution of the standard deviation of the shell $\sigma(t)$ obtained by solving the 3D GPE (1) numerically and correspond to the width of the radial density distributions plotted in figures 1(b)–(d).

Obviously, for $t_\mathrm{k} = 0$, the shell only spreads up freely, as depicted by the solid black line in figure 1(a). For $t_\mathrm{k} = 0.3\,\mathrm{ms}$ (red) we already observe a considerable slow down of the expansion, but in this case the shell width is still growing monotonically corresponding to a too short, undershooting lens. By further increasing the kick time the lens leads to an overshooting such that the width of the shell decreases directly after the delta-kick and then starts to grow once it reached its minimum extension. This behavior is exemplarily displayed for $t_\mathrm{k} = 1.0\,\mathrm{ms}$ (green). The compromise between both regimes is given by the optimal kick time $t_\mathrm{k} = 0.367\,\mathrm{ms}$ (orange) which only slightly overshoots and therefore keeps the shell width almost constant for several 100 ms of free expansion time. As we will show in more detail in the next section, there is indeed a certain value of t_k for a given delay time t_d leading to an optimal DKC performance such that the shell keeps its width for a long time without any external potential.

As the next step of our analysis, we quantitatively compare the results of the exact 3D numerical simulations with the prediction of the 1D model presented in section 2.3. In appendix B we have solved equation (10) with $f(t)$ given by equation (13) and derived the analytical formulas for the functions $\Lambda_1(t)$ and $\Lambda_2(t)$. With the help of equations (9) and (11) we then obtain the shell width $\sigma(t)$ and present its time dependence in figure 1(a) by dotted lines for the same values of t_k. As a result, the solid and dotted lines are very close to each other as long as the width stays below 40 μm, meaning that the 1D model describes the shell dynamics quite well in this regime. This behavior is in good agreement with the considerations of section 2.2 requiring the shell width to stay below the initial shell radius $r_0 = 60\,\mu\mathrm{m}$. Obviously this condition gets violated for the strongly overshooting lens (green curve) leading to deviations between the 1D model and the full 3D numerical simulation. In particular, the 1D model cannot describe the merging of the shell at the center of the coordinate system that leads to a change of slope for the numerically obtained solid green and black curves.

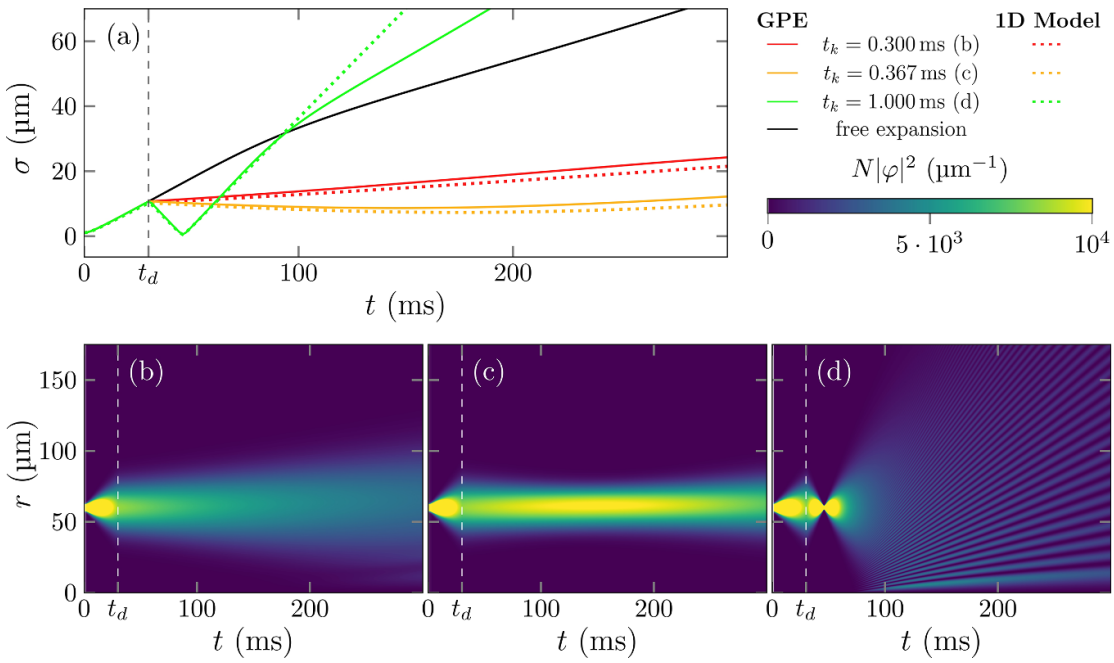

Figure 1. (a) Dependence of the shell width $\sigma(t)$ on the expansion time t obtained by numerical simulations of the 3D GPE, equation (1), (solid lines) compared to the analytical 1D model, equation (11), (dotted lines) for the time profile $f(t) = f_{\mathrm{DKC}}(t)$, equation (13), with delay time $t_\mathrm{d} = 30$ ms and different values of the kick time t_k including the purely free expansion (black). (b)–(d) Time evolution of the radial distribution $|\varphi(r,t)|^2 \equiv 4\pi r^2 |\psi(r,t)|^2$ for each of the nonzero values of t_k, respectively.

Moreover, slight deviations between the two approaches are due to the atom–atom interaction which is not taken into account by the 1D model. Indeed, neglecting the interaction requires $r_0/a_\mathrm{HO} \gg \sqrt{Na_s/a_\mathrm{HO}}$. For our parameters we have $r_0/a_\mathrm{HO} \approx 39$ and $\sqrt{Na_s/a_\mathrm{HO}} \approx 19$, such that the interaction still plays a minor, but relevant role.

Nevertheless, we can conclude that the 1D model predicts correct results as long as $\sigma(t) \ll r_0$ and the atom–atom interaction is not too strong.

3.2. Conditions for optimal lensing parameters

The results presented in figure 1 show that the DKC method works very well for keeping the width $\sigma(t)$ of a shell-shaped BEC at an almost constant value during the free evolution time t when slightly overshooting the lens. Now we are interested in obtaining specific conditions for the timings t_d and t_k to extend this time as long as possible in future experiments.

A suitable measure to characterize the performance of the lens is then given by the time interval Δt, which corresponds to the free expansion time after the lens that is required until the shell BEC reaches again the width it initially had at the time of the lens $t_\mathrm{d} + t_\mathrm{k}$. Formally, Δt can thus be defined by the relation

$$\sigma(t_\mathrm{d} + t_\mathrm{k} + \Delta t) = \sigma(t_\mathrm{d} + t_\mathrm{k}). \tag{14}$$

A comparison with figure 1 reveals that Δt is rather short for a heavily overshooting lens (green curve) and maximal for slightly overshooting (orange curve).

By inserting the analytical formulas for the functions $\Lambda_1(t)$ and $\Lambda_2(t)$, derived in appendix B, into equation (9), we obtain from equations (11) and (14)

$$\Delta t(t_\mathrm{d}, t_\mathrm{k}) = t_\mathrm{d} \frac{\omega_0 t_\mathrm{d} \sin(2\omega_0 t_\mathrm{k}) - 2\cos(2\omega_0 t_\mathrm{k})}{[\sin(\omega_0 t_\mathrm{k})]^2 + [\omega_0 t_\mathrm{d} \sin(\omega_0 t_\mathrm{k}) - \cos(\omega_0 t_\mathrm{k})]^2}. \tag{15}$$

We note that the right-hand side of equation (15) might be negative for certain values of t_d and t_k and we therefore set Δt equal to zero in these nonphysical situations.

For a given t_d, Δt reaches its maximum value when t_k is given by

$$t_\mathrm{k}^{(n)} = \frac{\pi n}{\omega_0} + \frac{1}{2\omega_0}\left[\frac{\pi}{2} + \arctan\left(\frac{2}{\omega_0 t_\mathrm{d}}\right) - \arctan\left(\frac{\omega_0 t_\mathrm{d}}{2}\sqrt{\omega_0^2 t_\mathrm{d}^2 + 4}\right)\right], \tag{16}$$

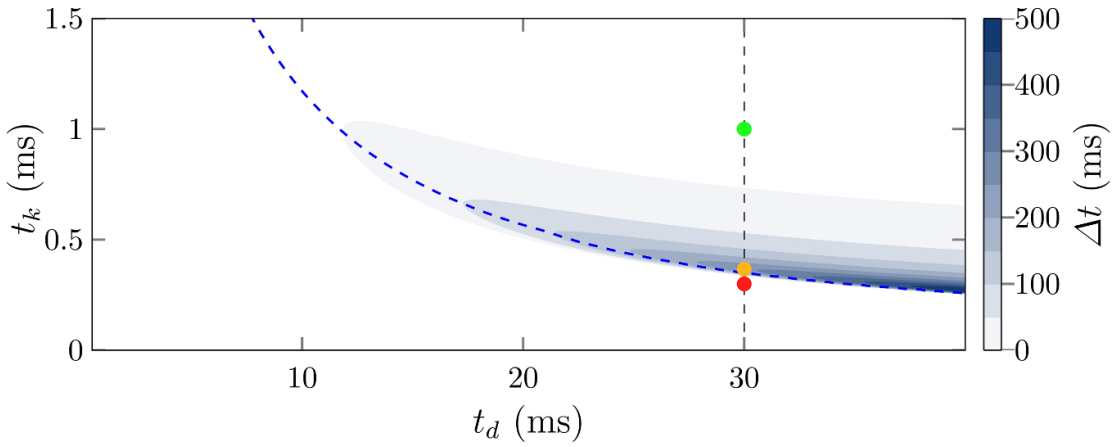

Figure 2. Contour plot of the time interval Δt, defined by equation (14) and given by equation (15), for different delay t_d and kick t_k times of the time profile $f_\mathrm{DKC}(t)$, equation (13). The three dots on the dashed black line mark the values of t_d and t_k corresponding to the subfigures (b)–(d) of figure 1. The blue dashed line identifies the optimal values of t_k, equation (16) with $n = 0$, as a function of t_d, resulting in the maximum value of Δt, equation (17).

with $n = 0, 1, 2\ldots$. The function $t_\mathrm{k}^{(n)}(t_\mathrm{d})$ is a multi-valued one, resulting from the fact that Δt, equation (15), is a periodic function of t_k with period π/ω_0. Here we consider only the case $n = 0$ yielding the maximum value

$$\Delta t_\mathrm{max}^\mathrm{DKC} \equiv \Delta t(t_\mathrm{d}, t_\mathrm{k}^{(0)}) = t_\mathrm{d}\sqrt{\omega_0^2 t_\mathrm{d}^2 + 4} \tag{17}$$

of the time interval Δt, equation (15), which is an increasing function of t_d.

As an example, for the delay time $t_\mathrm{d} = 30\,\mathrm{ms}$ used in figure 1, we obtain from equations (16) and (17) the optimal kick time $t_\mathrm{k}^{(0)} = 0.367\,\mathrm{ms}$ corresponding to the time interval $\Delta t_\mathrm{max} = 289\,\mathrm{ms}$.

In figure 2 the dependence of the time interval Δt, equation (15), on the delay time t_d and kick time t_k is visualized in a contour plot. In addition, the optimal kick time $t_\mathrm{k}^{(0)}$, equation (16), is also displayed by the dashed blue line. As a result, the collimation of a shell is better for larger t_d and smaller t_k times. However, in order to realize a rather thin and almost non-spreading shell for a long time, the free expansion time t_d should not be too large. In particular, for longer t_d, $\omega_0 t_\mathrm{d} \gtrsim 1$, the thickness of the shell σ increases linearly with t_d, namely $\sigma(t_\mathrm{d}) \approx a_\mathrm{HO}\,\omega_0 t_\mathrm{d}/\sqrt{2}$, as shown in appendix B. Hence, in order to ensure $\sigma(t_\mathrm{d}) \ll r_0$ with $r_0 \gg a_\mathrm{HO}$, the delay time t_d should obey the inequality $1 \lesssim \omega_0 t_\mathrm{d} \ll r_0/a_\mathrm{HO}$.

Consequently, a slowly spreading shell can be realized in an experiment by utilizing the standard DKC scheme, corresponding to the time-profile $f_\mathrm{DKC}(t)$, equation (13), of the trapping frequency, provided the delay time t_d and kick time t_k obey the optimal condition equation (16) with $n = 0$, displayed by blue dashed line in figure 2. In this case the shell width stays below a certain threshold during the time interval $\Delta t_\mathrm{max}^\mathrm{DKC}$, equation (17), enabling the study of freely floating shells for extended times. This scheme is particularly relevant for optically trapped shells which can be based on dual-species mixtures [2, 22].

3.3. Generalized matter-wave collimation

As we will discuss in more detail in section 4 it is not possible in all physical setups to switch off the trapping potential completely before performing the delta-kick pulse. Therefore, we now present a generalization of the conventional DKC technique that consists of the following three steps: (i) for $0 < t < t_\mathrm{d}$, the frequency $\omega_0 f(t)$ of the trap potential V, equation (3), is not set to zero but rather to a finite constant value $\omega_0 f_1$ with $f_1 > 0$, and (ii) for $t_\mathrm{d} < t < t_\mathrm{d} + t_\mathrm{k}$, the trapping frequency is again changed to another value $\omega_0 f_2$ with $f_2 > 0$, followed by (iii) turning off the trapping potential completely, for $t > t_\mathrm{d} + t_\mathrm{k}$. Hence, our general scheme is described by the time profile

$$f_\mathrm{gDKC}(t) = \begin{cases} f_1, & 0 < t \leqslant t_\mathrm{d} \\ f_2, & t_\mathrm{d} < t \leqslant t_\mathrm{d} + t_\mathrm{k} \\ 0, & t_\mathrm{d} + t_\mathrm{k} < t \end{cases} \tag{18}$$

of the trapping frequency. When choosing $f_1 = 0$ and $f_2 = 1$, sequence, equation (18), coincides with equation (13) and we obtain the previously discussed DKC scheme. The main idea behind this generalization is to induce width oscillations in the shell by changing the local trapping frequency and then switching off the trap at the point of maximum thickness in order to remove as much potential energy as possible, such that the cloud spreads slower afterwards.

By using these new parameters f_1 and f_2, we analyze how to best slow down the spreading of the shell-shaped BEC in comparison with the conventional DKC technique considered in section 3.2 when switching off the potential completely is not appropriate for the system under study. In order to find the optimal values for f_1 and f_2, we have again used the time interval Δt, defined by equation (14), and maximized it with respect to t_k and t_d for given values of f_1 and f_2. As a result, Δt achieves its maximal value

$$\Delta t_{\max}^{\mathrm{gDKC}}(f_1,f_2) = \frac{|f_1^4 - f_2^2|}{f_1^2 f_2^2 \omega_0} \tag{19}$$

at the optimal values

$$t_d^{(n_1)} = \frac{\pi}{2\omega_0 f_1}(2n_1 + 1) \tag{20}$$

and

$$t_k^{(n_2)} = \frac{1}{2\omega_0 f_2}\left[2\pi n_2 + \pi\Theta(f_1^2 - f_2) + \arccos\left(\frac{|f_1^4 - f_2^2|}{f_1^4 + f_2^2}\right)\right] \tag{21}$$

of the time t_k and t_d for given f_1, and f_2, where $n_{1,2} = 0, 1, 2\ldots$ and $\Theta(z)$ is the Heaviside step function, $\Theta(x > 0) = 1$ and $\Theta(x < 0) = 0$.

Now we can compare the efficiency of the generalized and standard DKC schemes to keep the shell width almost constant for longer free expansion time. Obviously, for realizing long-lived shells, one should avoid being close to the case $f_1^2 = f_2$ which leads to $\Delta t_{\max}^{\mathrm{gDKC}} = 0$ according to equation (19). Consequently, there are two main scenarios that promise large values for $\Delta t_{\max}^{\mathrm{gDKC}}$ depending on the relation between f_1 and f_2:

(i) For $f_1^2 \ll f_2$, we obtain $\Delta t_{\max}^{\mathrm{gDKC}} \approx 1/(\omega_0 f_1^2)$ and can distinguish two cases. The first case, $f_1^2 \ll f_2$ and $f_1 \ll 1$, resembles the standard DKC approach and the optimal values of t_d, equation (20), and t_k, equation (21), are given by $t_d^{(0)} \to \infty$ and $t_k^{(0)} \to 0$. They agree with the results derived in section 3.2. and presented in figure 2. Moreover, the maximal time interval $\Delta t_{\max}^{\mathrm{gDKC}} \approx 1/(\omega_0 f_1^2) = (2/\pi)^2 \omega_0 (t_d^{(0)})^2$ is approximately the same as the one of the standard DKC scheme, $\Delta t_{\max}^{\mathrm{DKC}} = \omega_0 t_d^2$, equation (17) for $\omega_0 t_d \gg 1$. In the second case, $f_1^2 \ll f_2$ and $f_1 \geqslant 1$, the generalized DKC scheme becomes less efficient compared to the standard one because the denominator of equation (19) grows when increasing f_1 beyond one. Physically, this case corresponds to inducing oscillations in a tighter trap compared to the initial one such that the quantum gas is compressed during the in-trap dynamics and more kinetic energy is left after release from the trap, leading to a faster spreading of the cloud.

(ii) For $f_1^2 \gg f_2$, we obtain $\Delta t_{\max}^{\mathrm{gDKC}} \approx (1/\omega_0 f_1^2)(f_1^2/f_2)^2$. As a result, for $f_1 \gg f_2$ and because of the large additional factor $(f_1^2/f_2)^2$, this novel regime of the generalized DKC scheme offers better performance compared to the first case of scenario (i). Here the main effect is obtained through oscillations in high frequency traps, with the delay time t_d being rather small and most of the collimation effect being due to the time t_k spent in the second trap.

4. Application to rf-dressed potentials

In this section we consider the case of rf-dressing for generating shell-shaped BECs and propose a realistic controlled expansion scheme enabling long-lived shells that takes into account all relevant experimental aspects.

4.1. rf dressed potentials

Nowadays, a promising approach to create shell-shaped BECs is to employ rf-dressed potentials [9, 16–19, 35]. In particular, we choose the commonly used model

$$V_{\mathrm{rf}}(r) = M_F \frac{g_F}{|g_F|}\sqrt{\left(\frac{m\omega_M^2}{2F}r^2 - \hbar\Delta\right)^2 + (\hbar\Omega)^2}, \tag{22}$$

where M_F is the momentum projection of the total momentum F of a dressed state in the hyperfine manifold with corresponding Landé factor g_F. The trap frequency ω_M of the static magnetic trap is chosen such that the potential of the highest trapped bare state is given by $V_{\mathrm{st}}(r) = m\omega_M^2/2$. Moreover, Δ is the detuning of the rf field with respect to the transition between neighboring bare states at the center of the trap, and Ω is the Rabi frequency proportional to the magnitude of the rf field.

The potential, equation (22), can be expanded around its minimum

$$r_0 = \left(2F\frac{\hbar\Delta}{m\omega_M^2}\right)^{1/2} \tag{23}$$

which yields

$$V_{\mathrm{rf}}(r) \approx M_F\frac{g_F}{|g_F|}\hbar\Omega + \frac{m\omega_0^2}{2}(r-r_0)^2 \tag{24}$$

with the local trap frequency

$$\omega_0 = \omega_M\left(\frac{2M_F g_F}{F|g_F|}\frac{\Delta}{\Omega}\right)^{1/2}. \tag{25}$$

Thus, the rf potential $V_{\mathrm{rf}}(r)$ can be approximated by a spherically symmetric harmonic oscillator shifted along the coordinate r by r_0, that is the rf potential has the form of equation (3). Therefore, we might utilize the results based on the standard DKC scheme to an rf-dressed potential. However, the DKC technique would not work, since a sudden switch off and on of the potential result in a mixture of different M_F states leading to atom losses in the shell. Furthermore, changing the trapping frequency ω_0 too fast in time is also detrimental since the M_F states need to follow the local magnetic field to feel the intended potential. To resolve these issues of employing an rf-dressed potential we present in the next section an adapted DKC approach that involves a continuous change of the trap frequency rather than sudden jumps.

4.2. Scheme and results for rf-dressed bubbles

To perform matter-wave lensing of a shell-shaped BEC initially created by rf-dressing with the potential (24) which has the form of equation (3), we model the time profile $f(t)$ with the following relation

$$f_{\mathrm{RF}}(t) = \begin{cases} 1-(1-f_1)\,t/t_{\mathrm{r}}, & 0 < t \leqslant t_{\mathrm{r}} \\ f_1, & t_{\mathrm{r}} < t \leqslant t_{\mathrm{r}} + t_{\mathrm{d}} \\ 0, & t_{\mathrm{r}} + t_{\mathrm{d}} < t \end{cases} \tag{26}$$

which is an adaption of the generalized DKC scheme discussed in section 3.3. Here the sequence starts with a linear ramp during the time $0 < t < t_{\mathrm{r}}$ to reduce the trap frequency from ω_0 to $f_1\omega_0$, which is then followed by keeping the trap frequency constant for the time t_{d} until the trap is finally turned off at $t = t_{\mathrm{r}} + t_{\mathrm{d}}$. The linear ramp ensures that the trap parameters are changed slow enough to not mix different M_F states. While keeping the trap constant afterwards with a reduced trap frequency the BEC will expand in that shallower trap and excite breathing oscillations. When the trap is switched off at the time the cloud has reached its maximum width, and therefore maximum potential energy, a huge amount of energy can be removed from the system leading to a slow free expansion of the cloud. This concept resembles the original DKC proposal by Chu *et al* [28].

We have studied the performance of the lensing scheme with $f(t) = f_{\mathrm{RF}}(t)$, equation (26), by carrying out numerical simulations of the 3D GPE (1) with ramping time $t_{\mathrm{r}} = 5\,\mathrm{ms}$ and different values of t_{d}. The results displayed in figures 3 and 4 are obtained for ^{87}Rb atoms in the state $|F=2, M_F=2\rangle$, the minimum of the trap $r_0 = 61\,\mu\mathrm{m}$, the initial trap frequency $\omega_0 = 2\pi\cdot 100\,\mathrm{Hz}$, $f_1 = 0.1$ and $|g_F| = g_F$. The time evolution of the shell width $\sigma(t)$ are displayed by the corresponding solid lines in figure 3(a) and the dashed lines are the results of the 1D model, presented in section 2, with the analytical formulas for $\Lambda_{1,2}(t)$ derived in appendix B. In addition, for each of the nonzero values of t_{d}, we show in figures 3(b)–(d) the time evolution of the radial distribution $|\varphi(r,t)|^2 \equiv 4\pi r^2|\psi(r,t)|^2$.

By increasing t_{d}, we observe a transition from an undershooting lens, $t_{\mathrm{d}} = 20\,\mathrm{ms}$, to an optimal collimation, $t_{\mathrm{d}} = 24.75\,\mathrm{ms}$, and finally to an overshooting lens, $t_{\mathrm{d}} = 30\,\mathrm{ms}$, for the adapted DKC scheme indicated by the red, orange, and green lines, accordingly. In the optimal case, $t_{\mathrm{d}} = 24.75\,\mathrm{ms}$, the shell keeps

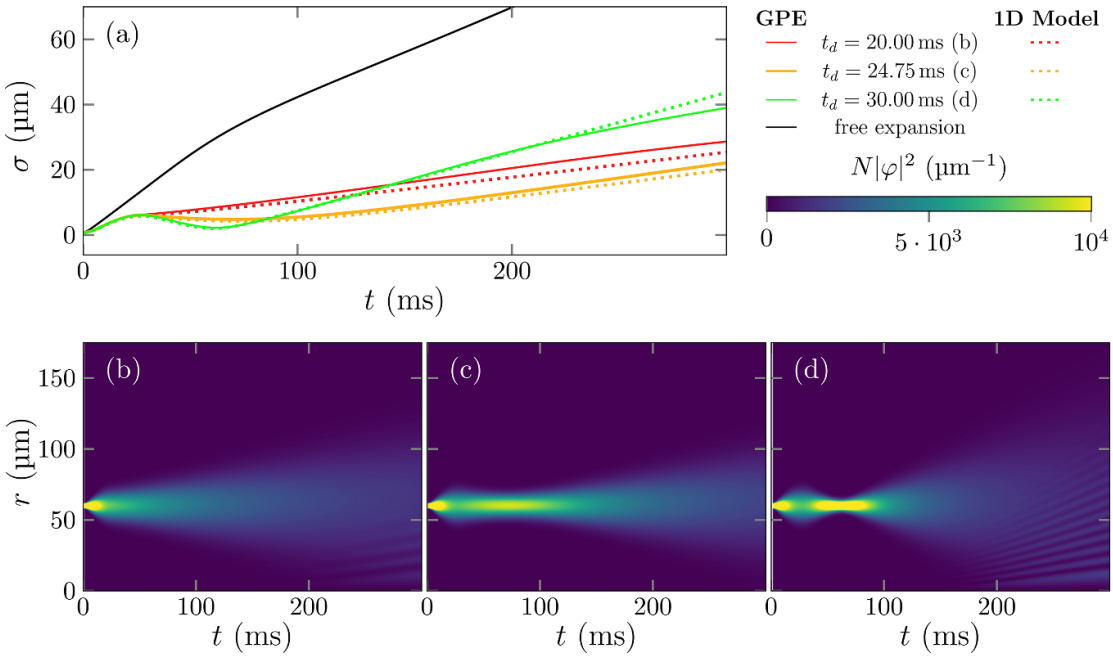

Figure 3. (a) Dependence of the shell width $\sigma(t)$, on the expansion time t obtained by solving numerically the 3D GPE, equation (1), (solid lines) compared to the results of the analytical 1D model, equation (11), (dotted line) with the time profile $f(t) = f_{\mathrm{RF}}(t)$, equation (26), for $f_1 = 0.1$, $t_r = 5$ ms, and different values of t_d. For comparison the black solid line results from the numerical solution of the 3D GPE with no ramp and $t_d = 0$. (b)–(d) Time evolution of the radial distribution $|\varphi(r,t)|^2 \equiv 4\pi r^2 |\psi(r,t)|^2$ for each of the nonzero values of t_d, respectively.

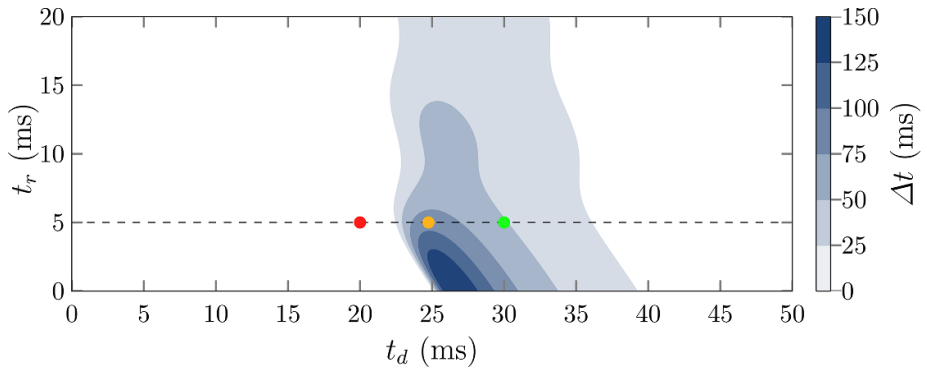

Figure 4. Contour plot of the time interval Δt, defined by equation (14), for different ramping t_r and delay t_d times of the time profile $f_{\mathrm{RF}}(t)$, equation (26). Dark colors indicate parameters leading to long free evolution times of the shell BEC. The three dots on the dashed black line mark the values of t_r and t_d corresponding to the subfigures (b)–(d) of figure 3.

its shape for around 100 ms which is sufficient time to manipulate the shell with external fields and observe its response during free expansion.

To obtain the optimal values of the ramping t_r and delay t_d times as functions of the other system parameters, we again maximize the time Δt, defined by equation (14). By employing the analytical solutions $\Lambda_{1,2}(t)$ derived in appendix B for the time profile $f_{\mathrm{RF}}(t)$, equation (26), we can express Δt as a function of t_r and t_d, as displayed in figure 4. Since Δt is a periodic function of t_d with period $\pi/(f_1\omega_0)$, the interval for t_d in figure 4 is restricted to one period. The three dots on the horizontal dashed line mark the values of t_r and t_d corresponding to subfigures (b)–(d) of figure 3, accordingly. As a result, the largest values of Δt occur for small ramping times and $t_d \approx \pi/(2f_1\omega_0) = 25$ ms. However, as discussed above, t_r should not be taken too small for the rf potential to avoid mixing the M_F states during the sequence.

4.3. Experimental feasibility

Now we discuss more precisely the experimental details of realizing the proposed adapted DKC scheme. The shell-shaped BEC of ^{87}Rb atoms in the state $|F=2, M_F=2\rangle$ with $|g_F| = g_F$ is prepared as the ground state of the rf potential with the trapping frequency $\omega_0 = 2\pi \cdot 100\,\mathrm{Hz}$ and the minimum $r_0 = 61\,\mu\mathrm{m}$. According to equations (23) and (25), this corresponds to $\Delta = 2\pi \cdot 20\,\mathrm{kHz}$, $\omega_M = 2\pi \cdot 50\,\mathrm{Hz}$, and $\Omega = 2\pi \cdot 10\,\mathrm{kHz}$. In general, there are several ways of realizing the linear ramp of the trapping frequency $f_{\mathrm{RF}}(t)$, equation (26), while keeping r_0 constant at the same time.

One option is to increase the Rabi frequency Ω over time. In this way, as follows from equation (25), the Rabi frequency at the end of the ramp is given by $\Omega(t_r) = \Omega(0)/f_1^2$. For $f_1 = 0.1$ and $\Omega(0) = 2\pi \cdot 10\,\mathrm{kHz}$, we obtain $\Omega(t_r) = 2\pi \cdot 1\,\mathrm{MHz}$ which seems to be too large even for state-of-the-art experiments with ultra-cold quantum gases. Additionally, the rotating wave approximation used for the rf-dressed potential equation (22) requires that the Rabi frequency is much smaller than the rf frequency. Thus, increasing Ω into the MHz regime is not an option and this approach is not sufficient on its own.

A second option is to keep Ω constant, but change both Δ and ω_M while keeping the ratio Δ/ω_M^2 constant during the ramp. Consequently, the static magnetic trap frequency ω_M and the rf detuning Δ need to follow the ramps

$$\omega_M^2(t) = \omega_M^2(0)\left[1 - (1-f_1)\frac{t}{t_r}\right] \tag{27}$$

and

$$\Delta(t) = \Delta(0)\left[1 - (1-f_1)\frac{t}{t_r}\right]. \tag{28}$$

With $\omega_M(0) = 2\pi \cdot 50\,\mathrm{Hz}$ and $\Delta(0) = 2\pi \cdot 20\,\mathrm{kHz}$, we obtain $\omega_M(t_r) = \sqrt{f_1}\omega_M(0) \approx 2\pi \cdot 15.8\,\mathrm{Hz}$ and $\Delta(t_r) = f_1\Delta(0) = 2\pi \cdot 2\,\mathrm{kHz}$ at the end of the ramp. These values correspond to typical experimental parameters and therefore a successful implementation of this scheme seems feasible.

To further elaborate on the feasibility of our proposed scheme, the influence of a non-spherically symmetric potential, for instance in the form of a cylindrical symmetric setup, needs to be taken into account. In the case that the local trap frequency, equation (25), is the same along the shell (angle independent), then our scheme can directly be applied even if the shell is not a sphere but an ellipsoid. If there is an angle-dependent local frequency which cannot be compensated by other means, then the expansion rate will vary over the size of the shell leading to a reduced free evolution time compared with the case of spherical symmetry. However, to improve the shell conservation time for non-spherically symmetric setups one could take advantage of the collective excitations of the shell similarly to proposals and experiments with filled BECs [32, 34].

5. Conclusion

In this article we have studied and adapted different matter-wave lensing schemes to conserve the shape of a shell-shaped BEC as long as possible during its free expansion. These techniques enable shell-shaped ultracold atomic gases to be a reliable platform for exploring many-body quantum phenomena on curved manifolds.

By considering the case where the shell radius is large enough in comparison with the shell width and for not too strong interaction strengths, we have employed an effective 1D model, using the 1D Schrödinger equation instead of the 3D GPE, to describe both the ground state and dynamics of a spherically symmetric shell-shaped BEC. This model allowed us to derive analytic results for an arbitrary time profile of the trapping frequency. In particular, for the conventional DKC scheme, corresponding to a step-wise change of the trapping frequency, we have obtained the optimal delay and kick times as functions of the experimental parameters for which the shell width keeps almost constant during its free dynamics. For typical parameters of state-of-the-art experiments with atomic BECs, expansion times of several hundred milliseconds can be reached.

In addition, we have proposed an adapted DKC scheme, where the trapping frequency is not changed suddenly but continuously. This technique is particularly important for shell-shaped BECs prepared with and controlled by an rf-dressed potential, where a step-wise change of the frequency would result in undesirable mixing of the different magnetic hyperfine sublevels. By obtaining optimal conditions for such a collimation scheme, we have shown that the shell structure can indeed be conserved for about one hundred milliseconds.

Thus, we are confident that the results presented in our paper will boost the accessibility of freely floating shell-shaped BECs independent of the employed experimental platform and drive future advancement in quantum many-body physics [36]. Furthermore, the discussed techniques can also be extended to rings and other non-trivially shaped BECs for many useful applications.

Data availability statement

The data cannot be made publicly available upon publication because no suitable repository exists for hosting data in this field of study. The data that support the findings of this study are available upon reasonable request from the authors.

Acknowledgments

We thank Naceur Gaaloul and Nathan Lundblad for fruitful discussions and helpful feedback about the manuscript. Moreover, we are thankful to Moritz Carmesin for discussion about the physics of the three dimensional harmonic oscillator. This project is supported by the German Space Agency (DLR) with funds provided by the Federal Ministry for Economic Affairs and Climate Action (BMWK) due to an enactment of the German Bundestag under Grants Nos. 50WM1862 and 50WM2245B (CAL).

Appendix A. From 3D GPE to 1D Schrödinger equation

In this appendix we show that for a spherically symmetric harmonic oscillator with a large radial shift of its minimum the ground state of a resulting shell-shaped BEC can be well described by a 1D Schrödinger equation instead of a full 3D GPE.

A.1. The role of atom–atom interaction in shell-shaped BECs

By introducing the dimensionless time, $\tau \equiv \omega_0 t$, and distance, $\rho \equiv r/a_{\mathrm{HO}}$, with the characteristic length $a_{\mathrm{HO}} \equiv \sqrt{\hbar/m\omega_0}$, as well as using the fact that the potential $V(\mathbf{r},t)$, equation (3), depends only on r, we arrive at the dimensionless 3D GPE

$$i\frac{\partial}{\partial\tau}\phi(\rho,\tau) = \left\{-\frac{1}{2}\frac{\partial^2}{\partial\rho^2} + \nu(\rho,\tau) + \frac{gN}{\rho^2}\left|\phi(\rho,\tau)\right|^2\right\}\phi(\rho,\tau) \tag{A.1}$$

for the dimensionless radial wave function $\phi(\rho,\tau) \equiv \sqrt{4\pi}a_{\mathrm{HO}}^{3/2}\rho\psi(\rho,\tau)$. The interaction constant $g = a_s/a_{\mathrm{HO}}$ and the dimensionless external potential $\nu(\rho,\tau)$ is given by

$$\nu(\rho,\tau) = \frac{1}{2}\left[f(\tau)\right]^2(\rho-\rho_0)^2 \tag{A.2}$$

with $\rho_0 \equiv r_0/a_{\mathrm{HO}}$.

Moreover, it is worth emphasizing that we consider only the spherically symmetric solution of the 3D GPE (1) and the normalization condition for $\phi(\rho,\tau)$ now reads

$$\int_0^\infty \mathrm{d}\rho\left|\phi(\rho,\tau)\right|^2 = 1. \tag{A.3}$$

Now we investigate the role of atom–atom interaction in a shell-shaped BEC, prepared as the ground state in the potential $\nu(\rho) = (\rho-\rho_0)^2/2$, that is $\nu(\rho,\tau)$, equation (A.2), with $f(\tau) = 1$. By applying the imaginary-time propagation method [37]to the time-dependent GPE (A.1), we have obtained the radial wave function $\phi_0(\rho)$ for the ground state of the corresponding time-independent GPE.

This wave function $\phi_0(\rho)$ is normalized according to condition (A.3) and determines the dependence of the kinetic, potential, interaction, and total energy per particles

$$\mathcal{E}_{\mathrm{kin}} \equiv \int_0^\infty \mathrm{d}\rho\phi_0^*(\rho)\left(-\frac{1}{2}\frac{\partial^2}{\partial\rho^2}\phi_0(\rho)\right) = \frac{1}{2}\int_0^\infty \mathrm{d}\rho\left|\frac{\partial}{\partial\rho}\phi_0(\rho)\right|^2, \tag{A.4}$$

$$\mathcal{E}_{\mathrm{pot}} \equiv \frac{1}{2}\int_0^\infty \mathrm{d}\rho(\rho-\rho_0)^2|\phi_0(\rho)|^2, \tag{A.5}$$

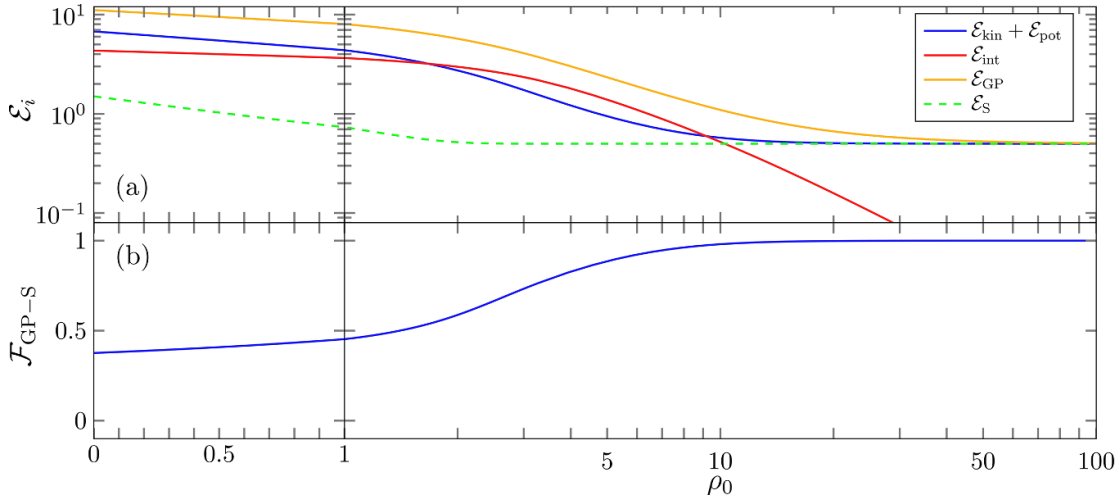

Figure A1. Dependence of the energies per particles $\mathcal{E}_{\mathrm{kin}}+\mathcal{E}_{\mathrm{pot}}$, $\mathcal{E}_{\mathrm{int}}$, and $\mathcal{E}_{\mathrm{GP}}$, defined by equations (A.4)–(A.7), as well as the overlap $\mathcal{F}_{\mathrm{GP-S}}$, equation (A.8), on the minimum position ρ_0 of the potential $(\rho-\rho_0)^2/2$. The solid lines in (a) and (b) are plotted for $g=0.0035$ and $N=10^5$, whereas the dashed green line corresponds to the total energy per particle $\mathcal{E}_{\mathrm{S}}$ of non-interacting atoms, that is $g=0$. The horizontal axis of both figures has two different scaling: a linear one, for $0\leqslant\rho_0\leqslant 1$, and a logarithmic one, for $1\leqslant\rho_0\leqslant 100$.

$$\mathcal{E}_{\mathrm{int}}\equiv\frac{1}{2}\int_0^\infty \mathrm{d}\rho\left(\frac{gN}{\rho^2}\right)|\phi_0(\rho)|^4, \tag{A.6}$$

$$\mathcal{E}_{\mathrm{GP}}\equiv\mathcal{E}_{\mathrm{kin}}+\mathcal{E}_{\mathrm{pot}}+\mathcal{E}_{\mathrm{int}}, \tag{A.7}$$

on the position ρ_0 of the trap minimum and the interaction constant g.

The energies $\mathcal{E}_{\mathrm{kin}}+\mathcal{E}_{\mathrm{pot}}$, $\mathcal{E}_{\mathrm{int}}$, and $\mathcal{E}_{\mathrm{GP}}$ are presented by corresponding solid lines in figure A1(a) for different values of ρ_0 with $N=10^5$ and $g=a_s/a_{\mathrm{HO}}=0.0035$. This value of g corresponds to ^{87}Rb atoms with scattering length $a_s=100a_0$ and trapping frequency $\omega_0=2\pi\cdot 50\,\mathrm{Hz}$, where a_0 is the Bohr radius.

For small ρ_0, $0\leqslant\rho_0\lesssim 10$, the total energy $\mathcal{E}_{\mathrm{GP}}(\rho_0,g)$, orange line, differs significantly from the total energy $\mathcal{E}_{\mathrm{S}}\equiv\mathcal{E}_{\mathrm{GP}}(\rho_0,0)$ per particle of non-interacting atoms, dashed green line, that is the energy of the ground-state in the potential $v(\rho)$, equation (A.2), obtained by solving the Schrödinger equation. However, for large ρ_0, $\rho_0>10$, the interaction energy $\mathcal{E}_{\mathrm{int}}(\rho_0,g)$, red line, is substantially reduced and both the total energy $\mathcal{E}_{\mathrm{GP}}(\rho_0,g)$ and the sum $\mathcal{E}_{\mathrm{kin}}+\mathcal{E}_{\mathrm{pot}}$, blue line, therefore approach $\mathcal{E}_{\mathrm{S}}$.

In addition, we have calculated the overlap

$$\mathcal{F}_{\mathrm{GP-S}}\equiv\int_0^\infty \mathrm{d}\rho\phi_0^*(\rho;g)\phi_0(\rho;0) \tag{A.8}$$

between the radial wave function $\phi_0(\rho;g)$ of the ground state of an interacting BEC and the one $\phi_0(\rho;0)$ of a non-interacting BEC, $g=0$. For $\rho_0\to\infty$, the overlap $\mathcal{F}_{\mathrm{GP-S}}$ as the function of ρ_0 approaches unity, as displayed in figure A1(b).

Hence, we have shown that for large enough values of ρ_0 both the energy and the wave function of the ground state of a BEC in the potential $v(\rho)=(\rho-\rho_0)^2/2$ can accurately be described by a 3D Schrödinger equation without the need to solve the full 3D GPE.

A.2. From 3D to 1D Schrödinger ground state

By using a 3D stationary Schrödinger equation, in this section we obtain the energy and the corresponding wave function of the ground state in the potential $v(\rho)=(\rho-\rho_0)^2/2$ for any value of ρ_0. In addition, we show that for large ρ_0 this state coincides with the one of a 1D harmonic oscillator.

The general solution of the 3D stationary Schrödinger equation

$$-\frac{1}{2}\frac{\partial^2}{\partial\rho^2}\phi(\rho)+\frac{1}{2}(\rho-\rho_0)^2\phi(\rho)=E\phi(\rho) \tag{A.9}$$

for the wave function $\phi(\rho)$ with the corresponding energy E is given by the linear superposition

$$\phi(\rho) = AD_{\nu}\left[\sqrt{2}(\rho-\rho_0)\right] + BD_{-1-\nu}\left[i\sqrt{2}(\rho-\rho_0)\right] \tag{A.10}$$

of the parabolic cylindrical functions $D_{\nu}(z)$ and $D_{-1-\nu}(iz)$ [38] with $\nu \equiv E - 1/2$.

The unknown constants A and B are determined by the boundary conditions

$$\lim_{\rho\to 0}\phi(\rho) = 0 \quad \text{and} \quad \lim_{\rho\to\infty}\phi(\rho) = 0, \tag{A.11}$$

giving rise to the wave function

$$\phi_n(\rho) = \mathcal{N}_n(\rho_0) D_{E_n-\frac{1}{2}}\left[\sqrt{2}(\rho-\rho_0)\right] \tag{A.12}$$

of the bound state ($n = 0, 1, 2, \ldots$) with the energy E_n, where we have used the fact that the function $D_{-1-\nu}(iz)$ diverges for $z \to +\infty$ [38]. In addition, the normalization constant $\mathcal{N}_n(\rho_0)$ is determined by equation (A.3) and reads

$$\mathcal{N}_n(\rho_0) = \left(\int_0^{\infty} \mathrm{d}\rho \left\{D_{E_n-\frac{1}{2}}\left[\sqrt{2}(\rho-\rho_0)\right]\right\}^2\right)^{-\frac{1}{2}}, \tag{A.13}$$

whereas the energy E_n is defined as a solution (with $E_n \geqslant 0$) of the transcendental equation

$$D_{E_n-\frac{1}{2}}\left(-\sqrt{2}\rho_0\right) = 0 \tag{A.14}$$

for any given $\rho_0 \geqslant 0$.

Here we are only interested in finding the dependence of the energy E_0 of the ground state on ρ_0. This is obtained by solving equation (A.14). However, this equation is quite complicated and we therefore derive analytical formulas for $E_0(\rho_0)$ in two limiting cases of (i) small and (ii) large values of ρ.

In the case of a small shell radius, $\rho_0 \to 0$, we insert the Taylor series for the function $D_{E_n-\frac{1}{2}}\left(-\sqrt{2}\rho_0\right)$ at its small argument into equation (A.14) and obtain the asymptotic expansion

$$E_0(\rho_0) \simeq \frac{3}{2} - \frac{2}{\sqrt{\pi}}\rho_0 + \frac{4}{\pi}\left[1 - \ln(2)\right]\rho_0^2 \tag{A.15}$$

for the ground-state energy $E_0(\rho_0)$ as $\rho_0 \to 0$, where we have omitted all terms of smaller orders. It means that the ground-state energy $E_0(\rho_0)$ approaches the one of a 3D spherically symmetric harmonic oscillator, $E_0(0) = 3/2$. In this limit, the corresponding ground-state wave function

$$\phi_0(\rho) \simeq \mathcal{N}_0(0) D_1\left(\sqrt{2}\rho\right) = \frac{2\rho}{\pi^{1/4}}\exp\left(-\frac{\rho^2}{2}\right) \tag{A.16}$$

also coincides with the one of the ground state of a 3D spherically symmetric harmonic oscillator. Here we have used the fact that $D_1(z) = z\exp(-z^2/4)$ [38] and calculated the normalization constant $\mathcal{N}_0(\rho_0)$, equation (A.13), for $\rho_0 = 0$.

In the opposite case of a shell with large radius, $\rho_0 \to \infty$, we insert the Taylor series for the function $D_{E_n-\frac{1}{2}}\left(-\sqrt{2}\rho_0\right)$, now at its large negative argument, into equation (A.14) and derive the asymptotic expansion

$$E_0(\rho_0) \simeq \frac{1}{2} + \frac{\rho_0}{\sqrt{\pi}}\mathrm{e}^{-\rho_0^2} \tag{A.17}$$

for the ground-state energy $E_0(\rho_0)$ as $\rho_0 \to \infty$.

Since $E_0(\rho_0) = 1/2$ as $\rho_0 \to \infty$, the wave function of the ground state

$$\phi_0(\rho) \simeq \Phi_{1\mathrm{D}}(\rho) = \mathcal{N}_0(\infty) D_0\left[\sqrt{2}\,(\rho-\rho_0)\right] = \frac{1}{\pi^{1/4}}\exp\left[-\frac{(\rho-\rho_0)^2}{2}\right] \tag{A.18}$$

approaches the one of the ground state of a 1D harmonic oscillator with the minimum located at ρ_0. In order to derive this result, we have used the relation $D_0(z) = \exp(-z^2/4)$ [38] and calculated again the corresponding normalization factor $\mathcal{N}_0(\infty)$, equation (A.13), for $\rho_0 \to \infty$.

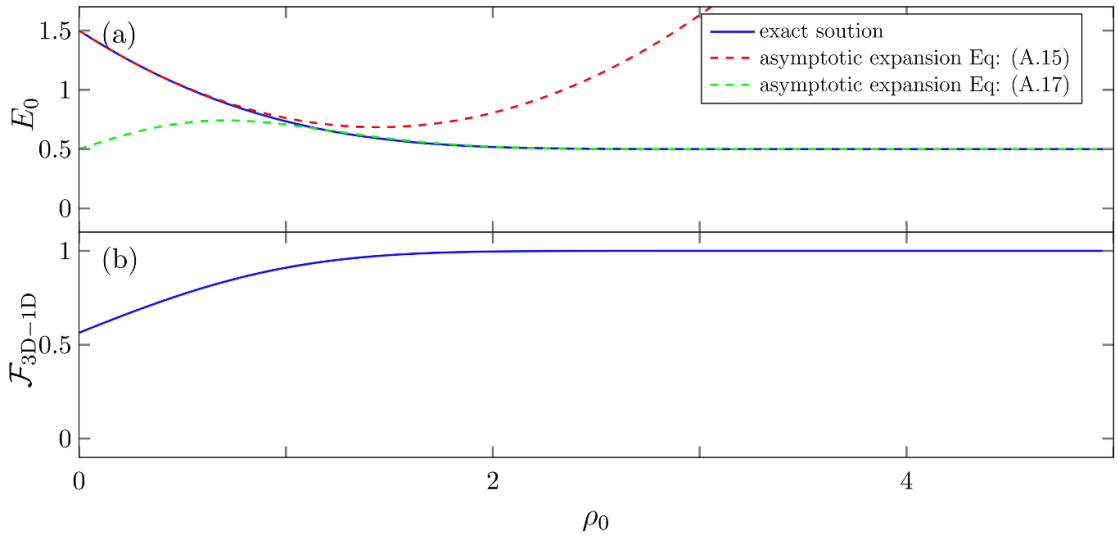

Figure A2. Dependence of the ground-state energy E_0, defined by equation (A.14), of the 3D Schrödinger equation, equation (A.9), and the overlap $\mathcal{F}_{3D-1D}$, equation (A.19), on the shift ρ_0 of the 3D spherically symmetric harmonic oscillator. The dashed red and green lines describe two asymptotic expansions for small, equation (A.15), and large, equation (A.17), values of ρ_0, accordingly.

To find the ground-state energy E_0 for any value of ρ_0, we solve equation (A.14) numerically and present this result in figure A2(a) by the solid blue line. For small and large values of ρ_0, this line perfectly reproduces the asymptotic behaviors given by equations (A.15) and (A.17), accordingly.

In addition, we have calculated the overlap

$$\mathcal{F}_{3D-1D} = \int_0^\infty d\rho \phi_0^*(\rho)\Phi_{1D}(\rho) \tag{A.19}$$

between the 3D wave function $\phi_0(\rho)$, equation (A.12), of the ground state and the corresponding 1D wave function $\Phi_{1D}(\rho)$, equation (A.18), and present its dependence on ρ_0 in figure A2(b). It shows in the clearest way that the ground state of the spherically symmetric harmonic oscillator with large shift ρ_0 is well described by the one of the shifted 1D harmonic potential.

As a result, according to the consideration presented in appendix A.1, our system is already in the regime of large ρ_0 and therefore we can model the trapping potential by the 1D shifted harmonic oscillator and study collimation of a shell-shaped BEC.

Appendix B. The effective 1D analytical model

In this appendix we consider the dynamics of the wave function, being initially prepared in a Gaussian shape, in the 1D harmonic oscillator with a time-dependent frequency.

B.1. Quantum dynamics of the 1D harmonic oscillator with time-dependent frequency

The solution of the 1D Schrödinger equation

$$i\frac{\partial}{\partial\tau}\varphi(\xi,\tau) = \left\{-\frac{1}{2}\frac{\partial^2}{\partial\xi^2} + \frac{1}{2}[f(\tau)]^2(\xi-\rho_0)^2\right\}\varphi(\xi,\tau) \tag{B.1}$$

for the wave function $\varphi(\xi,\tau)$, with $\xi \equiv x/a_{HO}$ being the dimensionless coordinate, $\xi \in (-\infty,\infty)$, governed by a harmonic oscillator with a time-dependent dimensionless frequency $f(\tau)$ is given by

$$\varphi(\xi,\tau) = \int_{-\infty}^{+\infty} dy\, G(\xi,\tau;\eta,0)\varphi(\eta,0), \tag{B.2}$$

where $\varphi(\xi,0)$ is the initial wave function.

The Green function

$$G(\xi,\tau;\eta,0)=\frac{1}{\sqrt{2i\pi\lambda(\tau)\lambda(0)\sin\left[\Phi(\tau)-\Phi(0)\right]}}\times\exp\left\{i\frac{\dot{\lambda}(\tau)}{2\lambda(\tau)}(\xi-\rho_0)^2-i\frac{\dot{\lambda}(0)}{2\lambda(0)}(\eta-\rho_0)^2\right\}\times\exp\left\{i\left[\frac{(\xi-\rho_0)^2}{2[\lambda(\tau)]^2}+\frac{(\eta-\rho_0)^2}{2[\lambda(0)]^2}\right]\cot\left[\Phi(\tau)-\Phi(0)\right]\right\}\times\exp\left\{-i\frac{(\xi-\rho_0)(\eta-\rho_0)}{\lambda(\tau)\lambda(0)\sin\left[\Phi(\tau)-\Phi(0)\right]}\right\} \tag{B.3}$$

is determined by the time-dependent functions

$$\Phi(\tau)=\int_0^\tau\frac{\mathrm{d}\tau'}{[\lambda(\tau')]^2} \tag{B.4}$$

and $\lambda(\tau)$ with its derivative $\dot{\lambda}(\tau)\equiv\mathrm{d}\lambda(\tau)/\mathrm{d}\tau$.

The function $\lambda(\tau)$ is the solution of the Ermakov equation

$$\frac{\mathrm{d}^2}{\mathrm{d}\tau^2}\lambda+[f(\tau)]^2\lambda=\frac{1}{\lambda^3} \tag{B.5}$$

with the initial condition $\lambda(0)=1$ and $\dot{\lambda}(0)=0$.

Taking the initial wave function $\varphi(\xi,0)$ in the form of the normalized wave function

$$\varphi(\xi,0)=\frac{1}{\pi^{1/4}}\exp\left(-\frac{(\xi-\rho_0)^2}{2}\right) \tag{B.6}$$

of the ground state of the harmonic oscillator, equation (B.1), with $f=1$, we perform the integration in equation (B.2) and arrive at

$$\varphi(\xi,\tau)=\left[\frac{1}{\sqrt{\pi}\lambda(\tau)}\right]^{1/2}\exp\left[-\frac{(1-i\lambda\dot{\lambda})}{2\lambda^2}(\xi-\rho_0)^2-\frac{i}{2}\Phi(\tau)\right]. \tag{B.7}$$

Here we have used the facts that $\Phi(0)=0$ and $\lambda(0)=1$.

B.2. Solution of the Ermakov equation

The solution of the general form of the Ermakov equation

$$\frac{\mathrm{d}^2}{\mathrm{d}\tau^2}\lambda+[f(\tau)]^2\lambda=\frac{a}{\lambda^3}, \tag{B.8}$$

with the initial conditions $\lambda(0)=\alpha$ and $\dot{\lambda}(0)=\beta$, where a, α and β are some constants, is given by

$$\lambda(\tau)=\left\{[\alpha\Lambda_1(\tau)+\beta\Lambda_2(\tau)]^2+\frac{a}{\alpha^2}[\Lambda_2(\tau)]^2\right\}^{\frac{1}{2}}. \tag{B.9}$$

Here $\Lambda_1(\tau)$ and $\Lambda_2(\tau)$ are two linearly independent solutions of the corresponding second-order linear differential equation

$$\frac{\mathrm{d}^2}{\mathrm{d}\tau^2}\Lambda+[f(\tau)]^2\Lambda=0 \tag{B.10}$$

with the initial conditions: $\Lambda_1(0)=1$ and $\dot{\Lambda}_1(0)=0$, or $\Lambda_2(0)=0$ and $\dot{\Lambda}_2(0)=1$.

In the case of the generalized scheme of DKC the profile $f(\tau)$ of the trapping frequency reads

$$f_{\mathrm{gDKC}}(\tau)=\begin{cases}f_1, & 0<\tau\leqslant\tau_\mathrm{d}\\ f_2, & \tau_\mathrm{d}<\tau\leqslant\tau_\mathrm{d}+\tau_\mathrm{k}\\ 0, & \tau_\mathrm{d}+\tau_\mathrm{k}<\tau\end{cases} \tag{B.11}$$

with the constants f_1 and f_2, where τ_d and τ_k are the dimensionless time delay and the kick duration, respectively.

By taking $a=1$, $\alpha=1$, and $\beta=0$ in equation (B.9) and solving equation (B.10) with $f(\tau)$, equation (B.11), we obtain the solution of equation (B.5) in the form

$$\lambda_{\mathrm{gDKC}}(\tau)=\sqrt{\left[\Lambda_1^{(\mathrm{gDKC})}(\tau)\right]^2+\left[\Lambda_2^{(\mathrm{gDKC})}(\tau)\right]^2}, \tag{B.12}$$

with $\Lambda_1^{(\mathrm{gDKC})}(\tau)$ and $\Lambda_2^{(\mathrm{gDKC})}(\tau)$ given by

$$\Lambda_1^{(\mathrm{gDKC})}(\tau)=\begin{cases}\cos(f_1\tau),\ 0<\tau\leqslant\tau_\mathrm{d}\\ \cos(f_1\tau_\mathrm{d})\cos[f_2(\tau-\tau_\mathrm{d})]-(f_1/f_2)\sin(f_1\tau_\mathrm{d})\sin[f_2(\tau-\tau_\mathrm{d})],\ \tau_\mathrm{d}<\tau\leqslant\tau_\mathrm{d}+\tau_\mathrm{k}\\ \cos(f_1\tau_\mathrm{d})\cos(f_2\tau_\mathrm{k})-(f_1/f_2)\sin(f_1\tau_\mathrm{d})\sin(f_2\tau_\mathrm{k})-\\ [f_2\cos(f_1\tau_\mathrm{d})\sin(f_2\tau_\mathrm{k})+f_1\sin(f_1\tau_\mathrm{d})\cos(f_2\tau_\mathrm{k})](\tau-\tau_\mathrm{d}-\tau_\mathrm{k}),\ \tau_\mathrm{d}+\tau_\mathrm{k}<\tau\end{cases} \tag{B.13}$$

and

$$\Lambda_2^{(\mathrm{gDKC})}(\tau)=\frac{1}{f_1}\begin{cases}\sin(f_1\tau),\ 0<\tau\leqslant\tau_\mathrm{d}\\ \sin(f_1\tau_\mathrm{d})\cos[f_2(\tau-\tau_\mathrm{d})]+(f_1/f_2)\cos(f_1\tau_\mathrm{d})\sin[f_2(\tau-\tau_\mathrm{d})],\ \tau_\mathrm{d}<\tau\leqslant\tau_\mathrm{d}+\tau_\mathrm{k}\\ \sin(f_1\tau_\mathrm{d})\cos(f_2\tau_\mathrm{k})+(f_1/f_2)\cos(f_1\tau_\mathrm{d})\sin(f_2\tau_\mathrm{k})-\\ [f_2\sin(f_1\tau_\mathrm{d})\sin(f_2\tau_\mathrm{k})-f_1\cos(f_1\tau_\mathrm{d})\cos(f_2\tau_\mathrm{k})](\tau-\tau_\mathrm{d}-\tau_\mathrm{k}),\ \tau_\mathrm{d}+\tau_\mathrm{k}<\tau,\end{cases} \tag{B.14}$$

respectively.

In the case of the rf-dressing scheme we model the profile $f_{\mathrm{RF}}(\tau)$ of the trapping frequency by

$$f_{\mathrm{RF}}(\tau)=\begin{cases}1-(1-f_1)(\tau/\tau_\mathrm{r}),\quad 0<\tau\leqslant\tau_\mathrm{r}\\ f_1,\quad \tau_\mathrm{r}<\tau\leqslant\tau_\mathrm{r}+\tau_\mathrm{k}\\ 0,\quad \tau_\mathrm{r}+\tau_\mathrm{k}<\tau,\end{cases} \tag{B.15}$$

where f_1 is the constant, $0<f_1<1$, τ_r and τ_k are the dimensionless ramping time and the kick duration, respectively.

The solutions $\Lambda_1^{(\mathrm{RF})}(\tau)$ and $\Lambda_2^{(\mathrm{RF})}(\tau)$ of equation (B.10) corresponding to $f_{\mathrm{RF}}(\tau)$ read

$$\Lambda_1^{(\mathrm{RF})}(\tau)=\begin{cases}(\pi/2)z_0^{3/4}z^{1/4}\left[Y_{-3/4}(z_0)J_{1/4}(z)-J_{-3/4}(z_0)Y_{1/4}(z)\right],\ 0<\tau\leqslant\tau_\mathrm{r}\\ \Lambda_1^{(\mathrm{RF})}(\tau_\mathrm{r})\cos[f_1(\tau-\tau_\mathrm{r})]+[\dot\Lambda_1^{(\mathrm{RF})}(\tau_\mathrm{r})/f_1]\sin[f_1(\tau-\tau_\mathrm{r})],\ \tau_\mathrm{r}<\tau\leqslant\tau_\mathrm{r}+\tau_\mathrm{k}\\ \Lambda_1^{(\mathrm{RF})}(\tau_\mathrm{r})\cos(f_1\tau_\mathrm{k})+[\dot\Lambda_1^{(\mathrm{RF})}(\tau_\mathrm{r})/f_1]\sin(f_1\tau_\mathrm{k})-\\ [\Lambda_1^{(\mathrm{RF})}(\tau_\mathrm{r})f_1\sin(f_1\tau_\mathrm{k})-\dot\Lambda_1^{(\mathrm{RF})}(\tau_\mathrm{r})\cos(f_1\tau_\mathrm{k})](\tau-\tau_\mathrm{r}-\tau_\mathrm{k}),\ \tau_\mathrm{r}+\tau_\mathrm{k}<\tau\end{cases} \tag{B.16}$$

and

$$\Lambda_2^{(\mathrm{RF})}(\tau)=\begin{cases}(\pi/2)z_0^{3/4}z^{1/4}\left[Y_{1/4}(z_0)J_{1/4}(z)-J_{1/4}(z_0)Y_{1/4}(z)\right],\ 0<\tau\leqslant\tau_\mathrm{r}\\ \Lambda_2^{(\mathrm{RF})}(\tau_\mathrm{r})\cos[f_1(\tau-\tau_\mathrm{r})]+[\dot\Lambda_2^{(\mathrm{RF})}(\tau_\mathrm{r})/f_1]\sin[f_1(\tau-\tau_\mathrm{r})],\ \tau_\mathrm{r}<\tau\leqslant\tau_\mathrm{r}+\tau_\mathrm{k}\\ \Lambda_2^{(\mathrm{RF})}(\tau_\mathrm{r})\cos(f_1\tau_\mathrm{k})+[\dot\Lambda_2^{(\mathrm{RF})}(\tau_\mathrm{r})/f_1]\sin(f_1\tau_\mathrm{k})-\\ [\Lambda_2^{(\mathrm{RF})}(\tau_\mathrm{r})f_1\sin(f_1\tau_\mathrm{k})-\dot\Lambda_2^{(\mathrm{RF})}(\tau_\mathrm{r})\cos(f_1\tau_\mathrm{k})](\tau-\tau_\mathrm{r}-\tau_\mathrm{k}),\ \tau_\mathrm{r}+\tau_\mathrm{k}<\tau,\end{cases} \tag{B.17}$$

respectively. Here $J_\nu(z)$ and $Y_\nu(z)$ are the Bessel functions of the first and second kind [38]. Moreover, we have introduced the function

$$z=z(\tau)=\frac{\tau_\mathrm{r}}{2(1-f_1)}\left[1-(1-f_1)\frac{\tau}{\tau_\mathrm{r}}\right]^2 \tag{B.18}$$

as well as notations $z_0=z(0)=\tau_\mathrm{r}/[2(1-f_1)]$ and $z_1=z(\tau_\mathrm{r})=\tau_\mathrm{r}f_1^2/[2(1-f_1)]$.

The constants $\Lambda_{1,2}^{(\mathrm{RF})}(\tau_\mathrm{r})$ and $\dot\Lambda_{1,2}^{(\mathrm{RF})}(\tau_\mathrm{r})$ are given by

$$\begin{aligned}\Lambda_1^{(\mathrm{RF})}(\tau_\mathrm{r})&=\frac{\pi}{2}z_0^{3/4}z_1^{1/4}\left[Y_{-3/4}(z_0)J_{1/4}(z_1)-J_{-3/4}(z_0)Y_{1/4}(z_1)\right]\\ \dot\Lambda_1^{(\mathrm{RF})}(\tau_\mathrm{r})&=-\frac{\pi}{2}z_0^{3/4}z_1^{1/4}f_1\left[Y_{-3/4}(z_0)J_{-3/4}(z_1)-J_{-3/4}(z_0)Y_{-3/4}(z_1)\right]\end{aligned} \tag{B.19}$$

and

$$\begin{aligned}\Lambda_2^{(\mathrm{RF})}(\tau_\mathrm{r})&=\frac{\pi}{2}z_0^{3/4}z_1^{1/4}\left[Y_{1/4}(z_0)J_{1/4}(z_1)-J_{1/4}(z_0)Y_{1/4}(z_1)\right]\\ \dot\Lambda_2^{(\mathrm{RF})}(\tau_\mathrm{r})&=-\frac{\pi}{2}z_0^{3/4}z_1^{1/4}f_1\left[Y_{1/4}(z_0)J_{-3/4}(z_1)-J_{1/4}(z_0)Y_{-3/4}(z_1)\right].\end{aligned} \tag{B.20}$$

ORCID iDs

Patrick Boegel https://orcid.org/0000-0002-3606-2452
Alexander Wolf https://orcid.org/0000-0002-3678-7808
Matthias Meister https://orcid.org/0000-0001-7210-8588
Maxim A Efremov https://orcid.org/0000-0001-6395-9663

References

[1] Carollo R A, Aveline D C, Rhyno B, Vishveshwara S, Lannert C, Murphree J D, Elliott E R, Williams J R, Thompson R J and Lundblad N 2022 Observation of ultracold atomic bubbles in orbital microgravity *Nature* **606** 281–6
[2] Jia F, Huang Z, Qiu L, Zhou R, Yan Y and Wang D 2022 Expansion dynamics of a shell-shaped Bose-Einstein condensate *Phys. Rev. Lett.* **129** 243402
[3] Turner A M, Vitelli V and Nelson D R 2010 Vortices on curved surfaces *Rev. Mod. Phys.* **82** 1301–48
[4] Padavić K, Sun K, Lannert C and Vishveshwara S 2020 Vortex-antivortex physics in shell-shaped Bose-Einstein condensates *Phys. Rev.* A **102** 043305
[5] Bereta S J, Caracanhas M A and Fetter A L 2021 Superfluid vortex dynamics on a spherical film *Phys. Rev.* A **103** 053306
[6] Kosterlitz J M 2016 Kosterlitz-Thouless physics: a review of key issues *Rep. Prog. Phys.* **79** 026001
[7] Tononi A, Pelster A and Salasnich L 2022 Topological superfluid transition in bubble-trapped condensates *Phys. Rev. Res.* **4** 013122
[8] Padavić K, Sun K, Lannert C and Vishveshwara S 2017 Physics of hollow Bose-Einstein condensates *Europhys. Lett.* **120** 20004
[9] Sun K, Padavić K, Yang F, Vishveshwara S and Lannert C 2018 Static and dynamic properties of shell-shaped condensates *Phys. Rev.* A **98** 013609
[10] Ríos J P 2020 *An Introduction to Cold and Ultracold Chemistry* (Cham: Springer)
[11] Naidon P and Endo S 2017 Efimov physics: a review *Rep. Prog. Phys.* **80** 056001
[12] Blume D 2012 Few-body physics with ultracold atomic and molecular systems in traps *Rep. Prog. Phys.* **75** 046401
[13] Olshanii M 1998 Atomic scattering in the presence of an external confinement and a gas of impenetrable bosons *Phys. Rev. Lett.* **81** 938–41
[14] Dunjko V, Moore M G, Bergeman T and Olshanii M 2011 Confinement-induced resonances *Advances in Atomic, Molecular and Optical Physics* vol 60, ed E Arimondo, P Berman and C Lin (New York: Academic) ch 10 pp 461–510
[15] Petrov D S, Holzmann M and Shlyapnikov G V 2000 Bose-Einstein condensation in quasi-2D trapped gases *Phys. Rev. Lett.* **84** 2551–5
[16] Zobay O and Garraway B M 2001 Two-dimensional atom trapping in field-induced adiabatic potentials *Phys. Rev. Lett.* **86** 1195–8
[17] Zobay O and Garraway B M 2004 Atom trapping and two-dimensional Bose-Einstein condensates in field-induced adiabatic potentials *Phys. Rev.* A **69** 023605
[18] Garraway B M and Perrin H 2016 Recent developments in trapping and manipulation of atoms with adiabatic potentials *J. Phys. B: At. Mol. Opt. Phys.* **49** 172001
[19] Perrin H and Garraway B M 2017 Trapping atoms with radio frequency adiabatic potentials *Advances in Atomic, Molecular and Optical Physics* vol 66, ed S F Yelin, E Arimondo and C C Lin (Saint Louis: Elsevier Science) pp 181–262
[20] Guo Y, Gutierrez E M, Rey D, Badr T, Perrin A, Longchambon L, Bagnato V S, Perrin H and Dubessy R 2022 Expansion of a quantum gas in a shell trap *New J. Phys.* **24** 093040
[21] Lundblad N, Carollo R A, Lannert C, Gold M J, Jiang X, Paseltiner D, Sergay N and Aveline D C 2019 Shell potentials for microgravity Bose-Einstein condensates *npj Microgravity* **5** 30
[22] Wolf A, Boegel P, Meister M, Balaž A, Gaaloul N and Efremov M A 2022 Shell-shaped Bose-Einstein condensates based on dual-species mixtures *Phys. Rev.* A **106** 013309
[23] Meister M and Roura A 2023 Efficient matter-wave lensing of ultracold atomic mixtures *Quantum Sci. Technol.* **8** 024001
[24] Timmermans E, Tommasini P, Hussein M and Kerman A 1999 Feshbach resonances in atomic Bose–Einstein condensates *Phys. Rep.* **315** 199–230
[25] Chin C, Grimm R, Julienne P and Tiesinga E 2010 Feshbach resonances in ultracold gases *Rev. Mod. Phys.* **82** 1225–86
[26] Tononi A, Cinti F and Salasnich L 2020 Quantum bubbles in microgravity *Phys. Rev. Lett.* **125** 010402
[27] Lannert C, Wei T-C and Vishveshwara S 2007 Dynamics of condensate shells: collective modes and expansion *Phys. Rev.* A **75** 013611
[28] Chu S, Bjorkholm J E, Ashkin A, Gordon J P and Hollberg L W 1986 Proposal for optically cooling atoms to temperatures of the order of 10^{-6} K *Opt. Lett.* **11** 73–75
[29] Ammann H and Christensen N 1997 Delta kick cooling: a new method for cooling atoms *Phys. Rev. Lett.* **78** 2088–91
[30] Kovachy T, Hogan J M, Sugarbaker A, Dickerson S M, Donnelly C A, Overstreet C and Kasevich M A 2015 Matter wave lensing to picokelvin temperatures *Phys. Rev. Lett.* **114** 143004
[31] Pandey S, Mas H, Vasilakis G and von Klitzing W 2021 Atomtronic matter-wave lensing *Phys. Rev. Lett.* **126** 170402
[32] Deppner C *et al* 2021 Collective-mode enhanced matter-wave optics *Phys. Rev. Lett.* **127** 100401
[33] Gaaloul N *et al* 2022 A space-based quantum gas laboratory at picokelvin energy scales *Nat. Commun.* **13** 2022
[34] Corgier R, Amri S, Herr W, Ahlers H, Rudolph J, Guéry-Odelin D, Rasel E M, Charron E and Gaaloul N 2018 Fast manipulation of Bose–Einstein condensates with an atom chip *New J. Phys.* **20** 055002
[35] Lesanovsky I, Hofferberth S, Schmiedmayer J and Schmelcher P 2006 Manipulation of ultracold atoms in dressed adiabatic radio-frequency potentials *Phys. Rev.* A **74** 033619
[36] Lundblad N *et al* 2022 Perspective on quantum bubbles in microgravity *Quantum Sci. Technol.* **8**
[37] Auer J, Krotscheck E and Chin S A 2001 A fourth-order real-space algorithm for solving local Schrödinger equations *J. Chem. Phys.* **115** 6841–6
[38] Olver F W J, Lozier D W and Boisvert R F and 2010 *NIST Handbook of Mathematical Functions* ed C W Clark (Cambridge: Cambridge University Press)